High ordered biomineralization induced by carbon nanoparticles in the sea urchin

Paracentrotus lividus

High ordered biomineralization induced by carbon nanoparticles in the sea urchin *Paracentrotus lividus*

Daniela Manno[1,2]**, Elisabetta Carata**[2]**, Bernadetta A Tenuzzo**[2]**,
Elisa Panzarini**[2]**, Alessandro Buccolieri**[1,2]**, Emanuela Filippo**[1,3]**,
Marco Rossi**[4]**, Antonio Serra**[1,3] **and Luciana Dini**[2]

[1] Interdepartmental Laboratory of Physics Applied to Materials Science, Italy
[2] DiSTeBA, Università del Salento, Lecce, Italy
[3] Dip. BBCC, Università del Salento, Lecce, Italy
[4] Dipartimento di Scienze di Base ed Applicate per l'Ingegneria, and Centro per le Nanotecnologie applicate all'Ingegneria, Sapienza Università' di Roma, Italy

E-mail: daniela.manno@unisalento.it

Abstract
A surprising and unexpected biomineralization process was observed during toxicological assessment of carbon nanoparticles on *Paracentrotus lividus* (sea urchin) pluteus larvae. The larvae activate a process of defense against external material, by incorporating the nanoparticles into microstructures of aragonite similarly to pearl oysters. Aiming at a better understanding of this phenomenon, the larvae were exposed to increasing concentrations of carbon nanoparticles and the biomineralization products were analyzed by electron microscopy, x-ray diffraction and Raman spectroscopy. In order to evaluate the possible influence of Sp-CyP-1 expression on this biomineralization process by larvae, analyses of gene expression (Sp-CyP-1) and calcein labeling were performed. Overall, we report experimental evidence about the capability of carbon nanoparticles to induce an increment of Sp-CyP-1 expression with the consequent activation of a biomineralization process leading to the production of a new pearl-like biomaterial never previously observed in sea urchins.

S Online supplementary data available from stacks.iop.org/Nano/23/495104/mmedia

(Some figures may appear in colour only in the online journal)

1. Introduction

It is well known that higher invertebrates and vertebrates, when exposed to contaminants (e.g. heavy metals), usually activate protection systems by increasing the expression of some proteins such as metallothioneins and heat shock proteins [1]. Some studies have considered the ability of sea urchin larvae to accumulate contaminants during development [2]. These contaminants can affect the biomineralization mechanisms, like in the cases of molluscs and echinoid larval stages [3]. Larval spicule formation is very interesting, because the larvae form an elaborate endoskeleton composed of two spicules, each one of which is a single crystal of magnesium-bearing calcite [4].

Mineralization, observed in many organisms, is a genetically regulated process and it is critical for correct development in many marine invertebrates. This process plays an essential role in the majority of metazoan taxa, because they construct a diversity of endo- and exo-skeletons by depositing biogenic solid minerals. For example, the mollusk shell is mainly composed of two layers, a prismatic layer and a nacreous layer. Both layers are in the form of calcium carbonate crystal; in particular, the prismatic layer forms calcite and the nacreous layer forms aragonite [5].

Sea urchins have five distinct mineralized skeletal elements: embryonic spicules, mature test, spines, lantern stereom and teeth. The spicules are transient structural elements whereas the spines and test plates are permanent. The teeth grow continuously. The mineral is a high magnesium calcite, but the magnesium content is different in each type of skeletal element, varying from 5 to 40 mol% Mg. The organic matrix creates the spaces and environments for crystal initiation and growth. The detailed mechanisms of crystal regulation are not known, but acidic and phosphorylated matrix proteins may be of special importance.

Biochemical studies, sequencing of the complete genome and high-throughput proteomic analysis have not yet provided insight into the mechanisms of crystallization, calcite composition and orientation applicable to all skeletal elements [6]. Using the recently sequenced sea urchin genome, Livingston *et al* conducted targeted searches for genes implicated in biomineralization of echinoderms and vertebrates [7] The identification of certain shared genes in the early biomineralization pathway of both of these groups led the authors to propose the presence of a common toolkit underlying the biomineralization mechanisms in distantly related taxa. Cyclophilins are peptidylprolyl cis–trans isomerases that are found in both prokaryotes and eukaryotes and facilitate protein folding. Although their specific role in calcification is not known, Livingston *et al* found eight cyclophilin genes expressed in sea urchin primary mesenchyme cells (PMCs), which are responsible for the initiation of spiculogenesis [8]. One of these genes, Sp-CyP-1, has been shown to be a member of the skeletogenic gene battery [9]. The fact that the gene is expressed throughout the phase of active skeletogenesis, which continues after the major period of cytological transformation through to the end of embryogenesis at 72 h, indicates that at least one major role is in the process of biomineral deposition and/or secretion.

The interaction of nanostructures and pluteus larvae is, at present, scarcely investigated. In addition, while the industrial applications of nanoparticles and nanostructured systems, like carbon nanostructures [10], metal oxides [11], liposomes, micelles and polymers [12], are increasing daily, up to now insufficient attention has been paid to possible environmental effects [13]. In particular, black carbon, produced from the incomplete combustion of vegetation (fires), fossil fuels and petrogenic processes (mineral, graphite), comprises a spectrum of related materials ranging from charred vegetation to refractory graphitic nanoparticles [14]. These nanoparticles, released into the atmosphere, impact on human health and the environment, and enter the aquatic environment, where they can affect the fate of other pollutants. Indeed, the peculiar physicochemical properties of nanomaterials also mean that they may have unique bioavailabilities [15] and other characteristics that make them potentially toxic to the environment and humans [16]. Notably, several studies have shown that black carbon is a significant component (up to 20%) of sedimentary organic carbon in the remote ocean [17] and could represent a significant carbon sink [18].

Sea urchins, being able to interact with various contaminants, are suitable candidates to control the level of contaminants of the sea coastal marine environment. Indeed, classical toxicity test protocols in bio-indicator species such as echinoderms are currently provided by international agencies and successfully applied for the biomonitoring and assessment of the health status of sea coastal environments (US EPA 2002; ASTM2004) [19].

In this work we analyze the interaction between carbon nanoparticles (with an average diameter of 13 nm and a dispersion of 12 nm) and pluteus larvae *Paracentrotus lividus* (sea urchin). In particular, we show that the larvae activate a defense process against external material: they incorporate the nanoparticles into aragonite microstructures. The larvae were exposed to increasing concentrations of carbon nanoparticles and the biomineralization products were analyzed by electron microscopy, x-ray diffraction and Raman spectroscopy. In order to evaluate the possible influence of Sp-CyP-1 expression on this biomineralization process by larvae, analyses of gene expression (Sp-CyP-1) and calcein labeling were performed. An increment of Sp-CyP-1 expression was observed with the consequent activation of a biomineralization process leading to the production of a new pearl-like biomaterial, never previously observed in sea urchins.

2. Experimental details

2.1. Synthesis

Carbon nanoparticles (C-NPs) were obtained via a one-step electrochemical method by the following route [20]. High purity graphite rod (SPI 99.99% purity, 5 mm diam.) was used as the anode and a stainless steel rod (Swagelok AISI 1016, 5 mm diam.) was used as the cathode. The electrodes were immersed in a beaker containing deionized water (Millipore Milli-*Q*, 18.2 $M\Omega$ cm) and kept at a distance of 10 mm. In the electrolysis process, the electric power applied to the electrodes was a constant voltage of 30 V. Simultaneously, the colloidal solution was forcedly dispersed by an ultrasonicator, which was of the flat type (Flexonic-1200-35/72/ 100G, Mirae Ultrasonic Tech., Korea). To prevent the aggregation of nanoparticles, the ultrasonicator was continuously operated at a power output of 1000 W with a frequency of 100 ± 5 kHz during the production of C-NPs.

2.2. Raman spectroscopy

Raman scattering measurements were obtained in the back-scattering geometry with a Renishaw spectrometer coupled to a Leica metallographic microscope. An argon-ion laser operated at a wavelength of 514.5 nm and a 10 mW incident power to avoid thermal effects provided the excitation. The Raman shifts were corrected by using silicon (111) reference spectra after each measurement.

To analyze the data, we decomposed the measured spectra using a multiple-peak fitting procedure. Satisfactory fits were achieved with the assumption of a Lorentzian central peak and the other peaks described by the spectral response functions of damped harmonic oscillators.

2.3. Transmission electron microscopy

The size and aggregation of C-NPs were analyzed by a Hitachi H-7100 transmission electron microscope operating at 100 kV, representing a suitable acceleration voltage to obtain a sufficient resolution and minimal radiation damage of the material. The TEM specimens were prepared by placing small droplets of the material to be examined onto standard carbon supported 600 mesh copper grids and drying slowly in air naturally. Both TEM images and selected area electron diffraction (SAD) were recorded.

2.4. From embryo culture to pluteus larvae

Adult *Paracentrotus lividus* sea urchins were collected along the coast of Salento. Eggs were fertilized and pluteus larvae were cultured at a dilution of 4.000 ml^{-1} in Millipore filtered sea water (MFSW) containing antibiotics, at 16–18 °C. The animals were induced to shed gametes by intracoelomic injection of 0.5 M KCl. The eggs were washed several times with filtered, natural seawater (SW), fertilized with a dilute suspension of sperm and cultured in SW in glass bowls. After 48–72 h it was possible to observe the formation of pluteus larvae.

2.5. Treatment with carbon nanoparticles

Four different glass bowls were used to add (i) no particles, control; (ii) 1×10^8 C-NPs ml^{-1}; (iii) 5×10^8 C-NPs ml^{-1}; and (iv) 5×10^9 C-NPs ml^{-1} to a suspension of pluteus larvae. After 24 h of exposure the larvae were collected by low-speed centrifugation.

2.6. RNA preparation and relative RT-PCR analysis

Total RNA was isolated according to the manufacturer's instructions using a PureLink^{TM} RNA Mini-Kit (Invitrogen) from collected pluteus larvae, frozen in liquid nitrogen and stored at −80 °C until use. Then, a single-step RT-PCR was carried out using a ThermoScript^{TM} RT-PCR System-skit (Invitrogen) according to the manufacturer's instructions. The sequences of the primers used were Pl-CyP1f 5′AGGTAAGAGCATCTACGGTGA3′ Pl-CyP1r 5′AACTTT GCCRAASACCACATG3′ Pl-S24f 5′CTGATCAGACCATG CTCTAAGGT-3′, Pl-S24r 5′CCTGATGTCGTCAGTACAA CGTA-3′.

The last amplification product was used as an internal reference control, as already reported [21]. The RT-PCR reaction was performed after denaturation for 2 min at 94 °C for 35 cycles as follows: 94 °C, 15 s; 55 °C, 30 s; 72 °C, 30 s. To calculate the relative Pl-CyP-1 expression we used the $\Delta \Delta$Ct method.

2.7. Calcein labeling

Because the rate of skeletal rod elongation varies with temperature, all pluteus larvae used for calcein labeling were cultured at 23 °C. Calcein was prepared as a 1.25 mg ml^{-1} stock solution in Instant Ocean (IO), pH 8.3, and stored at 4 °C. At selected stages, pluteus larvae were incubated for 1 h in IO containing 50 mg ml^{-1} calcein, then washed and transferred to fresh IO for 1 h. Labeled pluteus larvae were then fixed in 4% paraformaldehyde in IO at room temperature (RT) for 2 h. Pluteus larvae were examined with epifluorescence optics using a standard fluorescein filter set.

3. Results and discussion

3.1. Features of the C-NPs.

The carbon nanoparticles, obtained by the one-step electro-chemical method and used for all our experiments, were characterized by transmission electron microscope (TEM), Raman spectroscopy and x-ray diffraction in order to determine their features.

A typical TEM image of the synthesized carbon nanoparticles is shown in figure 1(a). The nanoparticles are mostly spherical in shape, with sizes in the range from 2 to 28 nm, and monodispersed, according to the distribution reported in the histogram of figure 1(b). The Gaussian curve with the best-fit parameters (average size $\langle d \rangle = 13$ nm and standard deviation $\sigma = 12$ nm) was superimposed on the histogram. The related selected area diffraction (SAD) pattern is shown in figure 1(c). The d-spacings, corresponding to the broadened rings, indicate that the carbon nanoparticles crystallized as graphite.

Figure 1(d) shows the x-ray diffraction pattern of the freshly synthesized C-NPs (solid line) together with the standard diffraction peak position and the relative intensity of hexagonal graphite (solid bar) [22]. Our pattern matches very well with the expected polycrystalline graphite. There are some small differences: from the peak position of the (002) line, the actual interlayer spacing turned out to be 0.34 nm, a value slightly larger than that of bulk graphite (0.3354 nm); in addition, the profiles of the 100 and 110 lines became asymmetric according to the Warren effect in turbostratic graphite [23]. These disparities may be due to the fact that the obtained C-NPs are very small and structurally disordered, in agreement with the features highlighted by the Raman spectroscopy.

The Raman spectrum obtained from the synthesized C-NPs and reported in figure 1(e) shows the typical features of low dimensional carbon structures. The amplitudes and locations of the G and 2D peaks, at 1584 and 2711 cm^{-1}, respectively, verify the sp^2 hybridization of the carbon bond in our nanoparticles [24] that, due to the large ratio of the G peak to the 2D one, are composed of multiple graphene layers [25] and have low range order recognizable by the presence of the D peak [26] at 1357 cm^{-1} and by the disorder-induced combination mode (D + G) at about 2940 cm^{-1} [27].

3.2. Morphological analysis of P. lividus pluteus larvae after interaction with carbon nanoparticles

The C-NPs were added to a suspension of pluteus larvae of*Paracentrotus lividus* in four different glass bowls (i) no particles, control; (ii) 1×10^8 C-NPs ml^{-1}; (iii) 5×10^8 C-NPs ml^{-1}; and (iv) 5×10^9 C-NPs ml^{-1}.

The pluteus larvae develop 48–72h after egg fertilization (as described in additional material available at stacks.iop.org/Nano/23/495104/mmedia). Figure 2(a) shows a typical pluteus larva, that represents an intermediate stage between the embryo and the adult produced during post-embryonic morphogenesis of *P. lividus* three days after fertilization. Pluteus has a size of about 5 mm, a gelatinous body with
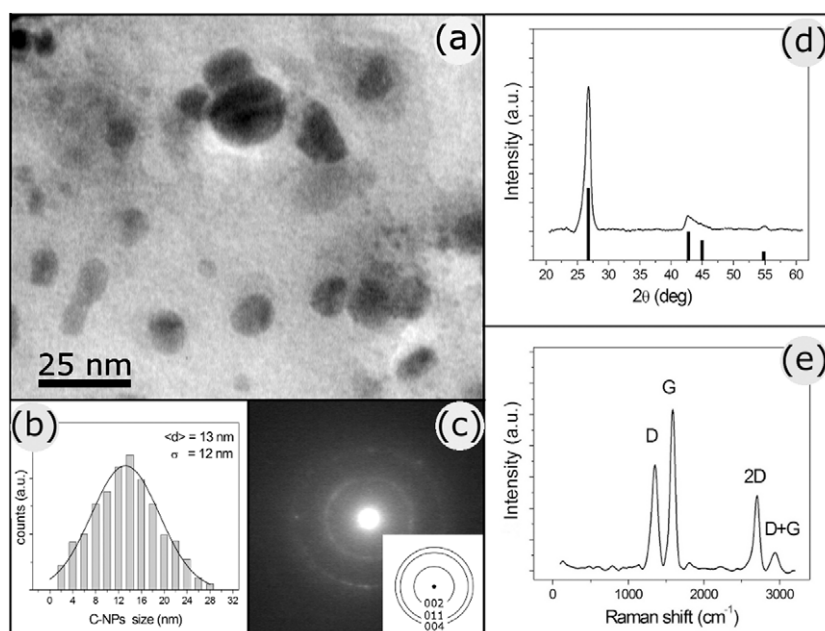
Figure 1. Features of the synthesized C-NPs. (a) TEM image, (b) nanoparticle distribution, (c) related selected area diffraction pattern and ring identification (inset), (d) XRD spectrum and (e) Raman spectrum.
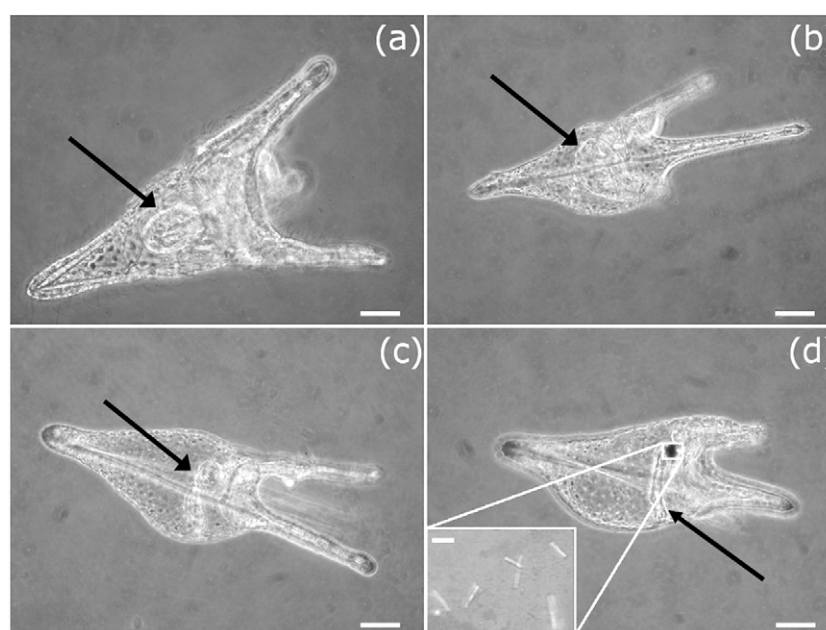

Figure 2. Pluteus larva of *P. lividus*, three days after fertilization. (a) Control, grown without administration of C-NPs. (b) Pluteus larva in the case of administration of 1×108 C-NPs ml^{-1}. (c) Pluteus larva in the case of administration of 5×10^8 C-NPs ml^{-1}. (d) Pluteus larva in the case of administration of 5×10^9 C-NPs ml^{-1}. Note the loss of the triangular shape and the regression of the arms with increasing concentration of C-NPs. The inset of picture (d) shows an optical magnification of the region of C-NP accumulation. In all pictures the bars are equal to 500 μm and the arrows indicate the gut localized at the center of the body.

4–6 arms and a typical bilateral symmetry. Under bright field microscopy, it is visible as a 'jelly' body having a triangular shape, as shown in figure 2(a). The gut, localized at the center of the body (arrowed), presents an ovoidal shape. The skeleton's spicules are perfectly adherent to the body wall and extend along the entire length of the larva. In the case of administration of small amounts of C-NPs (1×10^8 C-NPs ml^{-1}), morphological alteration of the larva

(figure 2(b)), consisting in the loss of the triangular shape, probably due to the detachment of the skeletal spicules from the body wall, can be observed. The digestive pouch expands, keeping the ovoidal shape. By increasing the amount of C-NPs in the culture medium (5×10^8 C-NPs ml^{-1}), the gut not only loses its original shape but also decreases its size drastically (figure 2(c)). In fact, this amount of C-NPs favors the detachment of the skeletal spicules from the larval body
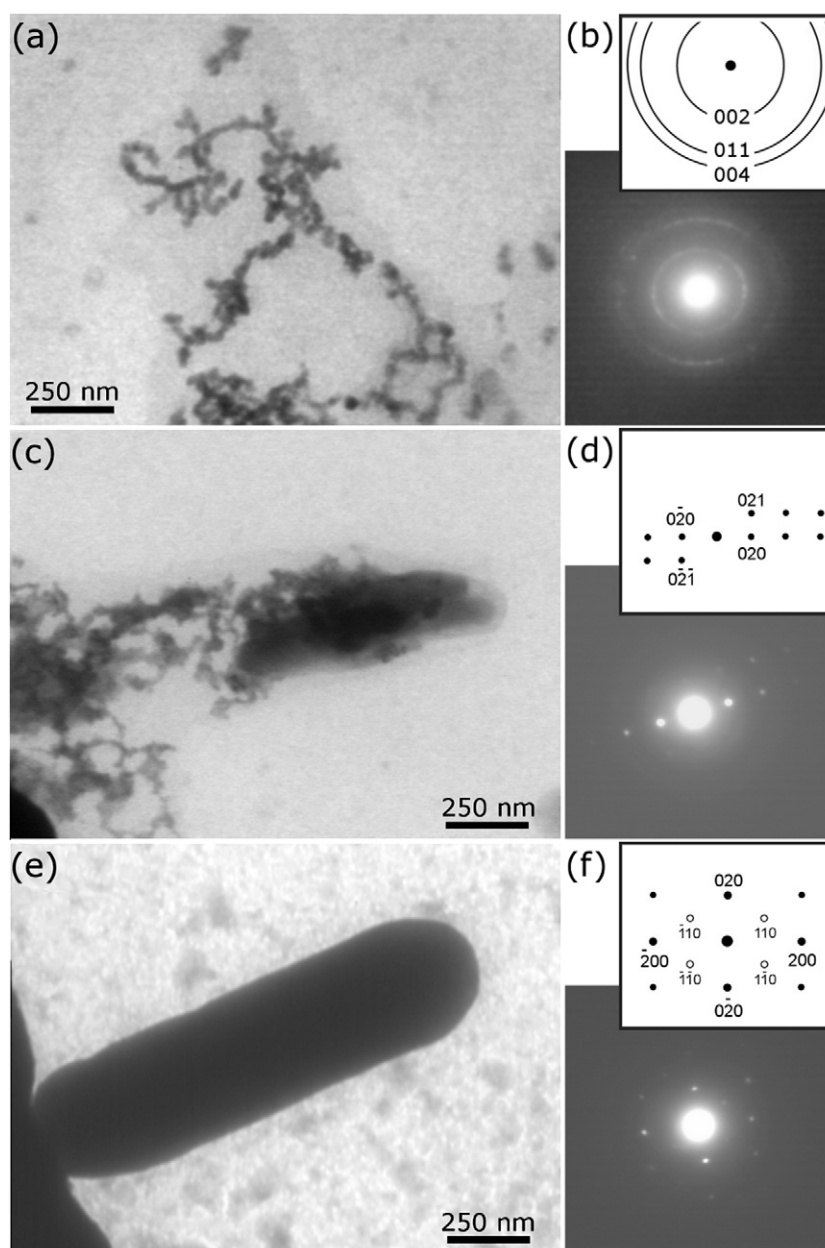
Figure 3. TEM images and related SAD patterns obtained with the material present in the gut of the pluteus larvae challenged with 1×10^8 C-NPs ml^{-1} (pictures (a) and (b)), 5×10^8 C-NPs ml^{-1} (pictures (c) and (d)) and 5×10^9 C-NPs ml^{-1} (pictures (e) and (f)). The evolution of the nanostructures' morphology and structure is indicative of a biomineralization process. The SAD pattern (b) is typical of nanostructured graphite, while the SAD patterns (d) and (f) are typical of aragonite, in agreement with the indexing shown.

wall, inducing a rounding of the same. In the treatment with a high quantity of C-NPs (5×10^9 C-NPs ml^{-1}), the loss of the triangular form is accompanied by regression of the arms and C-NP accumulation in the gut (figure 2(d)). The inset of figure 2(d) shows an optical magnification of the region of C-NP accumulation. Thin rectangular rods are unexplainably present in the gut.

3.3. The morphological and spectroscopical features of the material present in the gut

The features of the material present in the gut of the pluteus larvae, collected onto specific supports, were characterized by TEM and Raman spectroscopy.

Figure 3 shows typical TEM images and the related selected area electron diffraction patterns of the evolution of the C-NPs' morphology and structure, indicative of a biomineralization process. Indeed, once in contact with the C-NPs, pluteus larvae, most likely by activation of the biomineralization pathways, caused dose-dependent structural changes of the C-NPs.

The TEM image of figure 3(a) represents material collected from the pluteus larva of figure 2(b). In this case, it is evident that the C-NPs are no longer monodisperse, but are assembled in a randomly oriented nanoribbon. The related electron diffraction pattern (figure 3(b)) shows broadened rings similar to the ones obtained from the starting material.
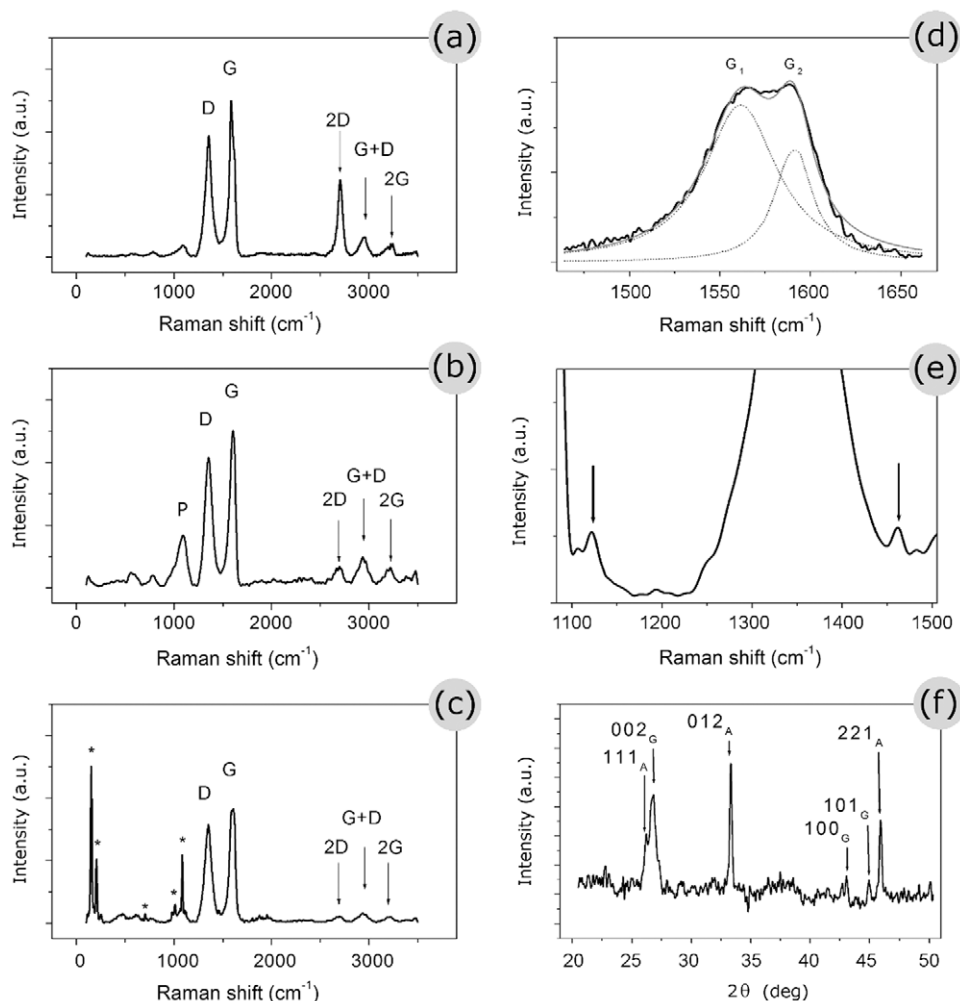
Figure 4. Raman spectra obtained from the material present in the gut of the pluteus larvae challenged with 1×10^8 C-NPs ml^{-1} (picture (a)), 5×10^8 C-NPs ml^{-1} (picture (b)) and 5×10^9 C-NPs ml^{-1} (picture (c)). In all these pictures, D, G, 2D, D + G and 2G mark carbon bands and asterisks the aragonite ones. The fine structure of the G band in (c) is reported in (d): the G band is interpolated by two Lorentzian curves centered at 1589 and 1618 cm^{-1} respectively. Picture (e) highlights the weak bands at 1124 and 1463 cm^{-1} of the spectra in (c) originated by protein C–N stretch and protein C–H$_2$, C–H$_3$ bending, respectively. The XRD (f) confirms the presence of aragonite in the gut.

The material collected from the pluteus larva of figure 2(c) shows the presence of more complex structures. Indeed, figure 3(c) shows a typical image of pluteus larva product: it is evident that the nanoribbons have been packed in a more complex structure, made of C-NPs assembled into a more ordered structure. The related electron diffraction pattern (figure 3(d)) shows a regular arrangement of spots that were indexed with the aid of web-based electron microscopy application software [28] and turned out to be aragonite [100] out of the zone axis. The final product of the process was collected from the pluteus larva of figure 2(d); it turned out to be a nanorod with rounded edges (figure 3(e)), very similar to the largest ones visible also in the optical microscope. The crystalline nature of this structure was unequivocally confirmed by the isolated spots in the related diffraction pattern (figure 3(f)). Also in this case the diffraction pattern was interpreted and turned out to be aragonite in the zone axis [001]. The spots were correspondingly indexed [28].

Raman spectroscopy performed on material from pluteus larvae gave the spectra shown in figure 4.

The Raman spectrum of figure 4(a), of the material collected from the pluteus larva of figure 2(b), indicates that the arrangement in a nanoribbon does not modify the structure of the C-NPs. The Raman spectrum of the material collected from the pluteus larva of figure 2(c) and shown in figure 4(b) results to be more different from the first one. In this case, an additional peak is present (P) and the 2D peak changes the structure.

Figure 4(c) shows the Raman spectrum of the sample collected from the pluteus larva of figure 2(d); in this spectrum two contributions are clearly visible: one due to graphitic nanostructured compounds and one due to calcium carbonate structures in a highly crystalline aragonite configuration. The contribution of C-NPs is evident in the presence of the bands D, G, 2G and G + D that are already present in the previous samples. In particular, the detailed examination of the structure of band G (figure 4(d)) reveals that band G can be interpolated by two Lorentzian curves centered at 1589 and 1618 cm^{-1}. This structure of band G is compatible with the presence of a nanoribbon of nanographite [29].

Table 1. Cyclophilin gene (Sp-CyP-1) homology results.

Accession	Description	Max identity (%)
AAR09898.1	Similar to Drosophila melanogaster CG2852 [*Drosophila yakuba*]	89
ADR66768.1	LP04623p [*Drosophila melanogaster*]	89
ABY64698.1	Cyclophilin G [*Armadillidium vulgare*]	93
XP_780268.1	Predicted: similar to peptidylprolyl isomerase B isoform 1 [*Strongylocentrotus purpuratus*] >ref|XP_001178998.1| Predicted: similar to peptidylprolyl isomerase B isoform 3 [*Strongylocentrotus purpuratus*]	93
XP_001175487.1	Predicted: similar to peptidylprolyl isomerase B [*Strongylocentrotus purpuratus*] >ref|XP_001178874.1| Predicted: similar to peptidylprolyl isomerase B isoform 1 [*Strongylocentrotus purpuratus*]	93
XP_802046.2	Predicted: similar to peptidylprolyl isomerase B isoform 5 [*Strongylocentrotus purpuratus*] >ref|XP_001178938.1| Predicted: similar to peptidylprolyl isomerase B isoform 2 [*Strongylocentrotus purpuratus*]	93
AAA35733.1	cyclophilin [*Homo sapiens*]	81
AAA52150.1	cyclophilin B [*Homo sapiens*]	81
ACB72457.1	PPIase B [*Bombyx mori*]	85

The aragonite [30] gives rise to very narrow and strong bands (highlighted with asterisks in figure 4(c)) at 153, 206 and 1085 cm^{-1}. The most intense band near 1085 cm^{-1} in the aragonite spectrum corresponds to the ν_1, symmetric stretching mode of the carbonate ions. The bands in the region of 100–300 cm^{-1} of the spectrum arises from translational and rotational modes of lattice vibrations. A very faint in-plane bending mode of the carbonate ions in aragonite occurs at about 700 cm^{-1}. These results indicate that the pluteus larva envelops the C-NPs in an aragonite rod. This hypothesis is supported by the presence of two weak bands at 1124 and 1463 cm^{-1}, more evident in the enlargement of figure 4(e), that are not assignable to vibrations of the carbonate ions in the aragonite crystal or carbon nanostructures. According to literature data [23], these vibrations can be originated by protein C–N stretch and protein C–H$_2$, C–H$_3$ bending, respectively. These bands may result from a diffuse matrix of protein that pervades the carbon matrix of the biogenerate structures.

The presence of aragonite in the biogenerated rods is also confirmed by XRD. Figure 4(f) shows the XRD spectrum obtained on the material collected from the pluteus larva of figure 3(d). The enlarged 002 graphite peak and the low and symmetrical 100 peak indicate lower sized C-NPs and ordered c stacking planes, according to Raman spectroscopy.

3.4. Sp-CyP-1 expression

In light of the above reported experimental evidence, it seemed helpful to evaluate the expression of the gene involved in the processes of biomineralization: the Sp-CyP-1. In fact, the cyclophilin is a peptidylprolyl cis–trans isomerase (PPIase) enzyme.

The observed formation of rods is probably the consequence of alteration of cyclophilin gene (Sp-CyP-1) expression during the development of pluteus larvae in the presence of C-NPs. In order to make this hypothesis clear we verified the presence of Sp-CyP-1 in *P. lividus*. The

DNA of the *P. lividus* was amplified using the degenerated primers Pl-CyP1f and Pl-CyP1r. These primers targeted a 238-nucleotide-long region highly preserved in different representative metazoan taxa. The amplicon was sequenced and aligned by PUB_Med blastx and the identities found are reported in table 1.

Interestingly, the cyclophilin gene of *P. lividus* has a high identity with cyclophilin of other animals. The higher identity is for the protein of another species of sea urchin, the *Strongylocentrotus purpuratus*.

3.5. mRNA levels of skeletogenic Sp-CyP-1

Sp-CyP-1 is executed only at the time of skeletal matrix deposition, 24 h after ingression of mesenchymal primary cells. Following its initial activation, Sp-CyP-1 continues to be expressed in skeletogenic cells throughout development.

The alteration of Sp-CyP-1 expression was measured in three independent experiments by real-time PCR. The results of RT-PCR, reported in figure 5(a), show that the expression of this gene is present in control pluteus and in the pluteus exposed to carbon nanoparticles. Interestingly, it is possible to observe an increase of expression independent of the nanoparticle concentration. This leads us to believe that the presence of C-NPs is sufficient to activate the gene overexpression.

3.6. Calcein labeling

After 24 h of exposure of larvae at three different concentrations of carbon nanoparticles, the pluteus larvae were collected and labeled with calcein, a polyanionic derivative of fluorescein that binds Ca^{2+} and other divalent cations [31]. The calcein is able to mark the sites in which there is active biomineralization and allows definition of a map of elongation sites of the endoskeleton *in vivo* [32].

In control plutei labeled with calcein, anterolateral rods, dorsoventral connecting rods, ventral transverse rods, postoral
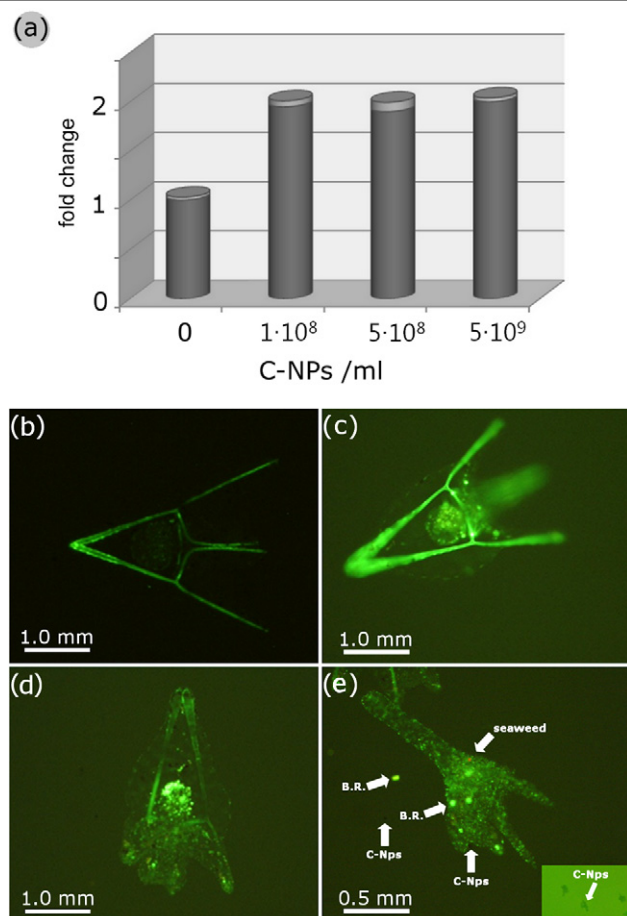
Figure 5. (a) Alteration of Sp-CyP-1 expression in pluteus larvae. The Sp-CyP-1 expression increased two fold over the control in a dose-independent manner. (a)–(e) Fluorescence microscope pictures of sea urchin plutei labeled with calcein: (b) 0 C-NPs ml^{-1}, control; (c) 1×10^8 C-NPs ml^{-1}; (d) 5×10^8 C-NPs ml^{-1} and (e) 5×10^9 C-NPs ml^{-1}. Picture (e) shows a very damaged larva, in which many new biomineralization rods, seems as white spots (arrow B.R.) are highlighted by calcein labeling. C-NPs appear as black spots, since they do not incorporate calcein (inset of picture (e)). The light gray autofluorescent spot (arrow seaweed) represents the food ingested by the pluteus, needed for the growth of the larva.

rods and body rods can be observed (figure 5(b)). In the larvae exposed to low concentrations of nanoparticles, it is possible to observe a few new starting sites of biomineralization in specific areas of the organism and represented by punctiform accumulations of calcein (figure 5(c)). The larvae exposed to medium concentrations of nanoparticles showed a greater number of new randomly formed sites of biomineralization while the endoskeleton was poorly marked; this behavior is justified by the action of calcein, which is able to mark the areas where there is a biological mineralization (figure 5(d)). In conclusion, plutei exposed to small quantities of C-NPs (figure 5(b)) barely feel the toxicity and thus the endoskeleton is labeled; conversely, plutei exposed to medium and high quantities (figures 5(c)–(d)) of C-NPs undergo an important nanoparticle-induced stress, and the normal biomineralization process is cut off and new sites of biomineralization are seen in zones different from normal conditions. In order to avoid mistakes of labeling we processed the carbon

nanoparticles with calcein, and, as already anticipated, we found that they were not fluorescently labeled, since in this systems there is not any metabolic activity (figure 5(e) inset). The nanoparticles remain always unlabeled; in fact when observing the larvae it is possible to note the presence of small black aggregates which correspond to accumulation of nanoparticles in the organisms (figure 5(e)).

The alteration of Sp-CyP-1 causes considerable induction of a dose-independent biomineralization process. As a consequence, more biomineralization sites can be seen in figure 5(d) than in figures 5(a)–(c); these differences can be mainly attributed to the different concentrations of carbon nanoparticles in the growth medium. Therefore, the concentration-independent overexpression of Sp-CyP-1 suggests that this gene expression is induced also by low amount of C-NPs, but a large number of nanoparticles is required for the mineralization of aragonite.

4. Conclusions

In this paper we highlight the interesting interaction between nanoparticles (C-NPs) and biological system (pluteus larvae of P. lividus), leading to the production of newly synthesized pearl like biomaterial, through the activation of one of the gene controlling skeletogenesis. In our experimental model, the nanoparticles did not bring about rapid death of the organism, as reported in other cases [33]; on the contrary, they represent a factor that interferes with correct development, whose phenomenological appearance is dramatic modification of the larva shape.

According to our data, we believe that the modified genetic regulation of biomineralization processes causes morphological alteration of pluteus larvae. The carbon nanoparticles firstly induce the organism to elaborate a strategy for self-defense. Electron microscopy results show that the pluteus packs the C-NPs in nanoribbons, then the nanoribbons are assembled into a more complex structure until aragonite nanorods are generated, and this process is 'dose dependent'. This behavior is peculiar to oysters that envelop the external agent in aragonite layers.

The biomineralization process is confirmed by Raman spectroscopy that evidences molecular vibrations due to a diffuse matrix of protein that pervades the carbon–aragonite matrix of the biogenerated structures.

This biomineralization process is activated by the Sp-CyP-1 gene, present in oysters. In this work we show that the Sp-CyP-1 gene is also present in *P. lividus* and that its expression is modulated by the presence of NPs.

Moreover, the analysis of gene expression (Sp-CyP-1) and calcein labeling well emphasizes the alteration of the process of biomineralization in the larvae. The results of the calcein labeling well support the data on gene Sp-CyP-1 alteration, whose increased expression coincides with an increased number of sites of biomineralization.

References

[1] Bauman J W, Liu J and Klaassen C D 1993 Production of metallothionein and heat-shock proteins in response to metals *Fundam. Appl. Toxicol.* **21** 15–22

[2] Radenac G, Fichet D and Miramand P 2001 Bioaccumulation and toxicity of four dissolved metals in Paracentrotus lividus sea urchin embryo *Mar. Environ. Res.* **51** 151–66

[3] Fabry V J, Seibel B A, Feely R A and James C 2008 Impacts of ocean acidification on marine fauna and ecosystem processes *ICES J. Marine Sci.* **65** 414–32

[4] Gilbert P U P A 2012 *J. Electron. Spectrosc. Relat. Phenom.* available online 22 June 2012, http://dx.doi.org/10.1016/j.elspec.2012.06.001

[5] Miyamoto H, Miyashita T, Okushima M, Nakano S, Morita T and Matsushiro A 1996 A carbonic anhydrase from the nacreous layer in oyster pearls *Proc. Natl. Acad. Sci. USA* **93** 9657–60

[6] Veis A 2011 Organic matrix-related mineralization of sea urchin spicules, spines, test and teeth *Front Biosci.* **16** 2540–60

[7] Livingston B T, Killian C E, Wilt H, Cameron A, Landrum M J, Ermolaeva O, Sapojnikov V, Maglott D R, Buchanan A M and Ettensohn C A 2006 A genome-wide analysis of biomineralization related proteins in the sea urchin Strongylocentrotus purpuratus *Dev. Biol.* **300** 335–48

[8] Yamasu K and Wilt F H 1999 Functional organization of DNA elements regulating SM30alpha, a spicule matrix gene of sea urchin embryos *Dev. Growth Differ.* **41** 81–91

[9] Amore G and Davidson E H 2006 cis-Regulatory control of cyclophilin, a member of the ETS-DRI skeletogenic gene battery in the sea urchin embryo *Dev. Biol.* **293** 555–64

[10] Terranova M L, Manno D, Rossi M, Serra A, Filippo E, Orlanducci S and Tamburri E 2009 Self-assembling of n-diamond nanocrystals into supercrystals *Cryst. Growth Des.* **9** 1245–9

[11] Filippo E, Serra A, Buccolieri A and Manno D 2010 Green synthesis of silver nanoparticles with sucrose and maltose: Morphological and structural characterization *J. Non-Crystalline Solids* **356** 344–50

[12] Fu G D, Li G L, Neoh K G and Kang E T 2011 Hollow polymeric nanostructures—synthesis morphology and function *Progr. Polym. Sci.* **36** 127–67

[13] Vishwakarma V, Samal S S and Manoharan N 2010 Safety and risk associated with nanoparticles—a review *J. Minerals Mater. Characterization Eng.* **9** 455–9

[14] Masiello C A 2004 New directions in black carbon organic geochemistry *Mar. Chem* **92** 201–13

[15] Oganesyan E A, Miroshnichenko I I, Vikhrieva N S, Lyashenko A, Yu A and Leshkov S 2010 Use of nanoparticles to increase the systemic bioavailability of trans-resveratrol *Pharmaceut. Chem. J.* **44** 74–6

[16] Dini L, Panzarini E, Serra A, Buccolieri A and Manno D 2011 Synthesis and *in vitro* cytotoxicity of glycans-capped silver nanoparticles *Nanomater. Nanotechnol.* **1** 58–63

[17] Lehmann J, Skjemstad J, Sohi S, Carter J, Barson M, Falloon P, Coleman K, Woodbury P and Krull E 2008 Australian climatecarbon cycle feedback reduced by soil black carbon *Nature Geosci.* **1** 832–5

[18] Bisiaux M M, Edwards R, Heyvaert A C, Thomas J M, Fitzgerald B, Susfalk R B, Schladow S G and Thaw M 2011 Stormwater and fire as sources of black carbon nanoparticles to lake tahoe *Environ. Sci. Technol.* **45** 2065–71

[19] Pinsino A, Della Torre C, Sammarini V, Bonaventura R, Amato E and Matranga V 2008 Sea urchin coelomocytes as a novel cellular biosensor of environmental stress: a field study in the Tremiti Island Marine Protected Area, Southern Adriatic Sea, Italy *Cell Biol. Toxicol.* **24** 541–52

[20] Serra A, Buccolieri A, Filippo E and Manno D 2012 Nanographite assembled films for sensitive NO_2 detection *Sensors Actuators* B **161** 359–65

[21] Zito F, Costa C, Sciarrino S, Poma V, Russo R, Angerer L M and Matranga V 2003 Expression of *univin* a TGF-β growth factor requires ectoderm–ECM interaction and promotes skeletal growth in the sea urchin embryo *Dev. Biol.* **264** 217–27

[22] http://rruff.info/

[23] Fujimoto H 2003 Theoretical x-ray scattering intensity of carbons with turbostratic stacking and AB staking structures *Carbon* **41** 1585–92

[24] Ferrari A C *et al* 2006 Raman spectrum of graphene and graphene layers *Phys. Rev. Lett.* **97** 187401

[25] Reina A, Jia X, Ho J, Nezich D, Son H, Bulovic V, Dresselhaus M S and Kong J 2009 Large area few-layer graphene films on arbitrary substrates by chemical vapor deposition *Nano Lett.* **9** 30–5

[26] Campos-Delgado J *et al* 2009 Resonant Raman study on bulk and isolated graphitic nanoribbons *Small* **5** 2698–702

[27] Campos-Delgado J *et al* 2008 Bulk production of a new form of sp^2 carbon: crystalline graphene nanoribbons *Nano Lett.* **8** 2773–8

[28] Zuo J M and Mabon J C 2004 Web-based electron microscopy application software: Web-EMAPS *Microsc. Microanal.* **10** 84–5 http://emapsmrluiucedu/

[29] Cancado L G *et al* 2004 Anisotropy in the Raman spectra of nanographite ribbons *Phys. Rev. Lett.* **93** 47403–7

[30] Urmos J, Sharma S K and Mackenzie F T 1991 Characterization of some biogenic carbonates with Raman spectroscopy *Am. Mineralogist.* **76** 641–6

[31] Wallach D F, Surgenor D M, Sodeberg J and Delano E 1959 Preparation and properties of 3,6-dihidroxy2,4-bis-[N,N'-di(carboxymethyl)-aminomethyl fluoran *Anal. Chem.* **31** 456–60

[32] Guss K A and Ettensohn C A 1997 Skeletal morphogenesis in the sea urchin embryo: regulation of primary mesenchyme gene expression and skeletal rod growth by ectoderm-derived cues *Development* **124** 1899–908

[33] Falugi C, Aluigi M G, Chiantore M C, Privitera D, Ramoino P, Gatti M A, Fabrizi A, Pinsino A and Matranga V 2011 Toxicity of metal oxide nanoparticles in immune cells of the sea urchin *Marine Environ. Res.* **76** 114–21